



# Bending of Soft Micropatterns in Elastohydrodynamic Lubrication Tribology

Y. Peng<sup>1</sup> · C. M. Serfass<sup>1</sup> · C. N. Hill<sup>1</sup> · L. C. Hsiao<sup>1</sup>

Received: 2 October 2020 / Accepted: 14 March 2021  
© Society for Experimental Mechanics 2021

## Abstract

**Background** Soft tribology is increasingly important in the design and engineering of materials used in robotics, haptics, and biomechanics studies. When patterned surfaces are part of a lubricated tribopair that undergoes sliding and compressive deformation, the patterns experience a bending strain that affects the lubrication film thickness and elastohydrodynamic friction. The contribution of bending patterns to soft tribology is not well understood because earlier studies focused on hard tribopairs with effectively flat surfaces.

**Objective** We investigate and model the differences in lubricated friction for poly(dimethyl siloxane) (PDMS) elastomer and PEGDA/alginate double network hydrogel patterns in order to determine the effect of height-to-width aspect ratio and bending angle on the elastohydrodynamic friction.

**Methods** Photoresists of two different viscosities are spin coated onto silicon substrates to fabricate molds with pattern heights ranging from 20  $\mu\text{m}$  to 50  $\mu\text{m}$ .

**Results** Tribological characterization of the tribopairs in the elastohydrodynamic lubrication regime shows that the patterns generate a friction peak that is independent of aspect ratio for short patterns but displays a “power-law fit” decrease with increasing aspect ratio for taller patterns. Two independent models are used to estimate the theoretical bending and deflection angles for the tribopairs.

**Conclusions** The decrease in lubricated friction is attributed to taller patterns having large bending angles and a reduced effective surface for fluid load bearing. Results suggest that the bending of micropatterns could be harnessed to engineer lubricated friction in a variety of applications.

**Keywords** Soft materials · Tribology · Textures

## Introduction

Tribological contacts involving soft surfaces are of increasing interest because of their ubiquity in biology, consumer products, and food science [1, 2]. Despite their prevalence, the tribology of soft materials is not fully understood and is often complicated by the presence of a lubricant film between the two deformable solid surfaces that make up a tribopair. This so-called elastohydrodynamic lubrication

(EHL) regime in tribology involves solid deformation of the surfaces by a thin fluid film, which imparts a pressure gradient in the velocity and flow-gradient planes [3–6]. The friction and wear of soft materials with flat surfaces has been extensively characterized and is relatively well understood, especially with Newtonian and shear thinning lubricants [7]. Nevertheless, the presence of micropatterns on the solid surfaces often results in different EHL friction coefficient values as compared to those observed with flat substrates [8–10]. These micropatterns are important in applications where friction modification is desired [11], although much remains unknown with regards to the optimization of texture dimensions [12, 13]. Earlier, our group developed a scaling framework that incorporates Reynolds' equations and elasticity to predict the EHL friction coefficients of soft textured tribopairs, including that of robotic and human fingers [14]. The increase in friction coefficient was most pronounced

---

Y. Peng and C. M. Serfass have contributed equally to this work.

---

✉ L. C. Hsiao  
lilian\_hsiao@ncsu.edu

<sup>1</sup> Department of Chemical and Biomolecular Engineering,  
North Carolina State University, 911 Partners Way, Raleigh,  
NC 27695-7905, USA

when the flow of the lubricant is perpendicular to the striped textures, suggesting that micro-EHL arises from changes in the fluid pressure field and flow direction caused by the patterns. The frictional contributions from pattern bending become especially important when tall, slender patterns are used (Fig. 1). Their tendency to bend under applied shear stresses leads to changes in the thickness of the lubricant film, which in turn couples to the viscous and elastic dissipation of the tribopair.

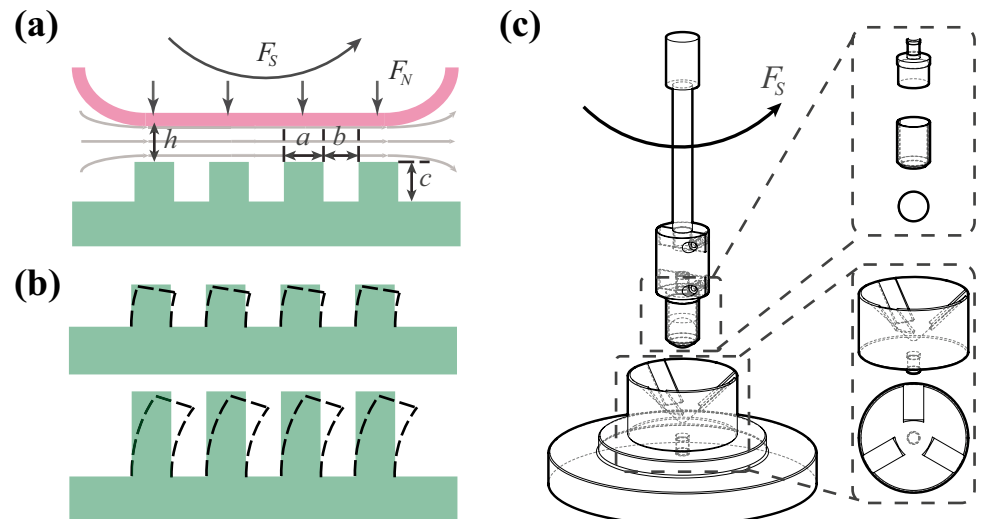
The majority of tribological mechanics to date has focused on compressive deformation with little attention being given to shear or bending stresses imparted by the fluid film on the solid surfaces. This is likely because EHL tribology was originally developed for hard metal surfaces that were considered flat at the micron scale [15, 16]. In this case, the length scales of any nanoscale asperities are insignificant compared to the range of lubrication forces in squeeze and shear flows, which decay inversely and tangentially with respect to the separation distance [17]. A slip-flow length is often incorporated to pinpoint the relative importance of hydrodynamics to roughness [18].

Bending is most prevalent when the aspect ratio of height to width is large (Fig. 1(b)). For example, the bending strain of slender papillae on our tongues is proportional to shear stresses from maceration. It is thought that papillae amplify shear stresses for mechanical receptors located at their bases, allowing for enhanced sensory perception [19, 20]. Bending is also believed to play a role in shear drag reduction. An investigation on leaves exposed to high winds found that those with the longest petioles, which were able to bend the most, experienced lower drag forces and were less likely to suffer damage [21]. While the flows examined in this study were at high Reynolds number ( $Re$ ), where inertial effects dominate, drag reduction through bending has also been

observed in low  $Re$  systems, where viscous forces dominate [22]. Low  $Re$  flows are common in EHL because the thickness of most lubricant films spans nanometers to microns [7].

Studies focused on low  $Re$  flows have shown that bending of surface patterns is proportional to the pattern height and flow rate [20, 22]. When the bending strain of a pattern is low (< 1%), the deflection can be approximated using Euler–Bernoulli beam theory, which treats the pattern as a linear elastic beam [23–25]. This allows for stress–strain engineering in many interesting applications. Duprat et al. measured the bending modulus of unanchored gel rods by bridging them between two constricting features in a confined microfluidic channel and measuring their maximum deflection at the center of the channel [23]. The same principle was applied to an anchored beam by Wexler et al., who obtained the elastic modulus by measuring the beam tip deflection [24]. Lauga et al. developed a model of the filiform papillae of tongues by treating them as beams that deform in the linear regime [19]. They deduced that the filiform papillae likely serve as mechanosensors themselves or amplify strains for easier detection by mechanosensors at the base of the tongue. Young et al. found that the bending of beam-like cilia hairs in mammalian cells resulted in shear forces being maximized at the base of the hairs, suggesting that one of the biological purposes of cilia is to activate mechanosensors through strain amplification [25]. Using these bending principles, Thomazo et al. developed a biomimetic tongue-palate system with the aim of quantifying texture perception [20]. In this system, the tips of the elastomeric papillae were marked with a fluorescent dye, allowing their deflection to be imaged using a rheo-microscope. Their experimental results were in agreement with Lauga's model [19]. Later, they varied the surface density of beams and found that increased surface density of pillars decreased the bending deflection [26].

**Fig. 1** (a) Sketch of PDMS–PDMS tribopair and experimental accessory used in this study, where relevant geometrical and force parameters are indicated. The lubricant is glycerol. (b) Illustration of bending mechanics for patterns with different height-to-width aspect ratios when a shear stress at the free end is present. (c) Ball-on-three-plates tribo-rheological accessory, in which the top ball and three substrates are in three-point contacts. The ball rotates and slides against three bottom substrates with friction force  $F_S$



In cases where large height-to-width aspect ratios lead to correspondingly large bending strains, linear beam theories begin to fail and more complex models may have to be employed [22, 27, 28]. Axtmann et al. developed an empirical model based on measurements and numerical simulations of flexible rods in viscous drag up to  $Re=60$  [27]. Alvarado et al. used a Taylor-Couette cell and observed that, at higher flow velocities, nonlinear beam bending resulted in a power-law reduction in the shear stress [22]. These results elucidate the importance of pattern bending in the mechanical properties of systems with low  $Re$  flows. Because EHL friction is the ratio of the shear and normal stresses exerted on the solid surfaces, a better understanding of bending mechanics is critical to modeling and understanding the EHL tribology of soft patterned materials.

In this study, we investigate the effect of pattern aspect ratio on the EHL tribology of patterned elastomeric tribopairs. Soft lithography is used to fabricate elastomer substrates with micron-sized stripes and aspect ratios ranging from 0.4 to 2.3 (Fig. 1(a)). Figure 1(a) shows a representative illustration of the side view of tribological contacts, in which the substrates become deformed by large lubrication pressures. The millimeter-scale curvature of the top ball geometry give rise to a non-uniform, asymmetric pressure differential within the gap [5, 29]. Here, the reported film thickness represents an average value across the gap. Stribeck curves are obtained using a stress-controlled rheometer with a ball-on-three-plate tribology accessory, where glycerol is used as the lubricant to generate fully flooded conditions. The data analysis focuses on the micro-EHL friction peaks that are observed with such patterns. At these peaks, the EHL contribution from bending is decoupled from compression and used to estimate the theoretical bending angles of the patterns. Results suggest that bending is indeed correlated with the aspect ratio of surface patterns, where taller and thinner patterns give rise to increased

bending angles and a corresponding reduction in the micro-EHL friction coefficient.

## Materials and Methods

### Fabrication of Micropatterned Poly(dimethyl Siloxane) (PDMS) Elastomers

All materials are obtained from Sigma-Aldrich and used without purification unless otherwise stated. Patterned silicon wafers are produced by standard lithography. Photomasks for soft lithography are designed in AutoCAD and printed by FineLine Imaging. The micropatterns used in this study are stripes with dimensions  $a$  and  $b$ , where  $a$  refers to the width of the raised stripes ( $15 \mu\text{m} \leq a \leq 55 \mu\text{m}$ ), and  $b$  is the width between the valleys ( $b=35 \mu\text{m}$ ). We use two types of SU-8 photoresist with different viscosities (SU-8 2050 and SU-8 2025) and vary the spin speed  $s$  in rotations per minute ( $s_{\text{SU-8 2050}} = 2500, 3000, 3500, 4000 \text{ RPM}$ ;  $s_{\text{SU-8 2025}} = 3500, 4000 \text{ RPM}$ ) of a spin coater obtain micropatterns with different heights ( $c = 50 \mu\text{m}, 35 \mu\text{m}, 29 \mu\text{m}, 25 \mu\text{m}, 23 \mu\text{m}, 20 \mu\text{m}$ , Fig. 2(a), (b)). Figure 2(a) shows the calibration curve for pattern height where  $c$  decreases with increasing  $s$ . Because SU-8 2050 (12,900 cSt) has a higher viscosity than SU-8 2025 (4500 cSt), it produces taller patterns at the same  $s$ . The resulting patterned silicon wafers serve as molds for fabricating poly(dimethyl siloxane) (PDMS) substrates.

Soft PDMS patterned substrates are produced by casting 12 g of Sylgard 184 (Dow Corning, curing agent to base ratio = 1:10 w/w%) over a micropatterned wafer and crosslinking the precursor at 70 °C overnight. The Young's modulus of the cured PDMS substrates is  $E = 2 \text{ MPa}$  [30]. We cut the micropatterned PDMS substrate into 0.6 cm × 1.5 cm × 1.9 mm slabs for tribological testing. To fabricate the PDMS balls for PDMS-PDMS tribopairs, we

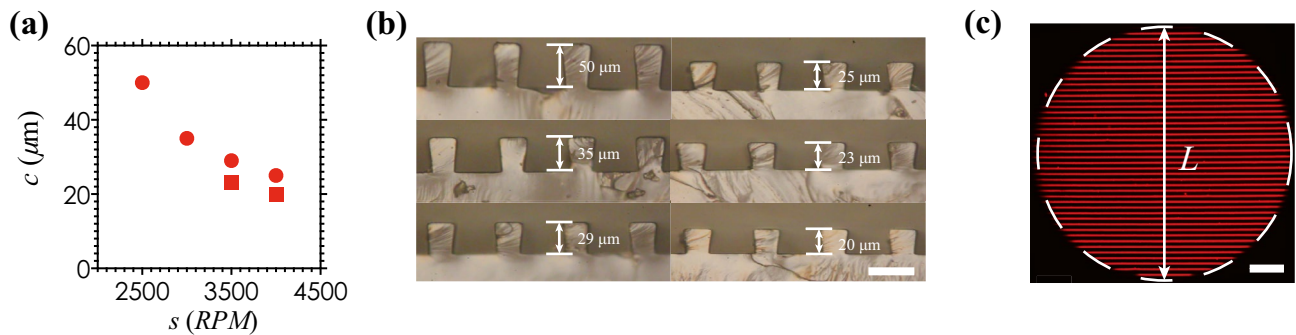


**Fig. 2** (a) Plot of pattern height as a function of the spin coating speed using the photoresists SU-8 2050 (solid red circles) and SU-8 2025 (solid red squares). (b) Representative optical micrographs that show PDMS patterned elastomers with pattern dimensions  $a=25 \mu\text{m}$ ,  $b=55 \mu\text{m}$ , and various heights. Scale bar = 50  $\mu\text{m}$ . (c) Representa-

tive confocal laser micrograph of static dry contact area on patterned substrate where  $a=25 \mu\text{m}$ ,  $b=55 \mu\text{m}$ . The compression experiment is conducted at  $\text{FN}=1.5 \text{ N}$ . Dashed circle indicates the total contact area with a diameter of  $L=2.9 \text{ mm}$ . Scale bar = 0.5 mm

inject the Sylgard 184 precursor into a custom stainless-steel mold heated at 70 °C overnight. The radius of crosslinked PDMS ball is 1.27 cm.

### Fabrication of Micropatterned Double Network (DN) Hydrogel

Micropatterned poly(ethylene glycol) diacrylate (PEGDA)/alginate double network (DN) hydrogel substrates are made via replica molding. Alginic acid and PEGDA are obtained from Sigma-Aldrich and used without further purification. In order to prepare the patterned hydrogel, the PEGDA and alginate monomers are crosslinked in two steps. Both alginate and PEGDA are mixed with deionized water at a concentration of 5% and 40%, respectively. A mixture of the monomers is obtained by mixing PEGDA and alginate monomer solutions in 10:1 w/w% ratio. The photoinitiator 2-hydroxy-2-methylpropiophenone or Darocur (Sigma-Aldrich) is added to the mixture at 0.5:99.5 w/w %. The mixture is stirred for 10 min before being transferred to a glass vial. The entire container is covered in aluminum foil and allowed to tumble at 25 rpm for at least 24 h. After 24 h, the sample is placed in a centrifuge at 10,000 rpm for 20 min. The sample is then poured slowly (to prevent entrapment of bubbles) into the middle of the PDMS mold and placed under UV light for one hour ( $\lambda=254$  nm). Once completely crosslinked, the hydrogel sample is removed from the PDMS mold and soaked in a 1 M calcium chloride solution for 24 h. DN hydrogel plates for tribological testing are cut using a razor blade.

### Tribological Characterization

We conduct tribological experiments at room temperature on a stress-controlled rheometer (DHR-2, TA Instruments) fitted with a ball-on-three-plates geometry (Fig. 1(c)). This tribological accessory involves three patterned slabs inserted at a 45° angle in the bottom wells and a PDMS ball that serves as the top contact. The PDMS ball is lowered against the three slabs to make contact at a fixed normal force of  $F_N=1.5$  N. Pure glycerol is used to generate fully flooded conditions at all three contact points. Patterns are oriented perpendicular to the direction of sliding. The relative sliding velocity  $\omega$  ranges from 1 rad/s to 80 rad/s. Steady state data points are collected for 40 values of  $\omega$  within this range. Each data point is obtained by averaging the values obtained over 25 s. The friction force  $F_S$  is obtained from the torque captured by the torque sensor within the instrument. The Reynolds number  $Re=\rho Uh/\eta$  represents the ratio of inertial to viscous forces, where  $U$  is the average sliding velocity,  $\rho$  is the density of glycerol ( $\rho=1.26$  g/cm<sup>3</sup>),  $h$  is the separation distance between the PDMS ball and the top of the micropatterns, and  $\eta$  is the dynamic viscosity of glycerol ( $\eta=1.412$  Pa·s). The calculated  $Re$  is  $\leq 2$ , suggesting that laminar flow is maintained throughout all experiments.

### Contact Area of Micropatterned Surfaces

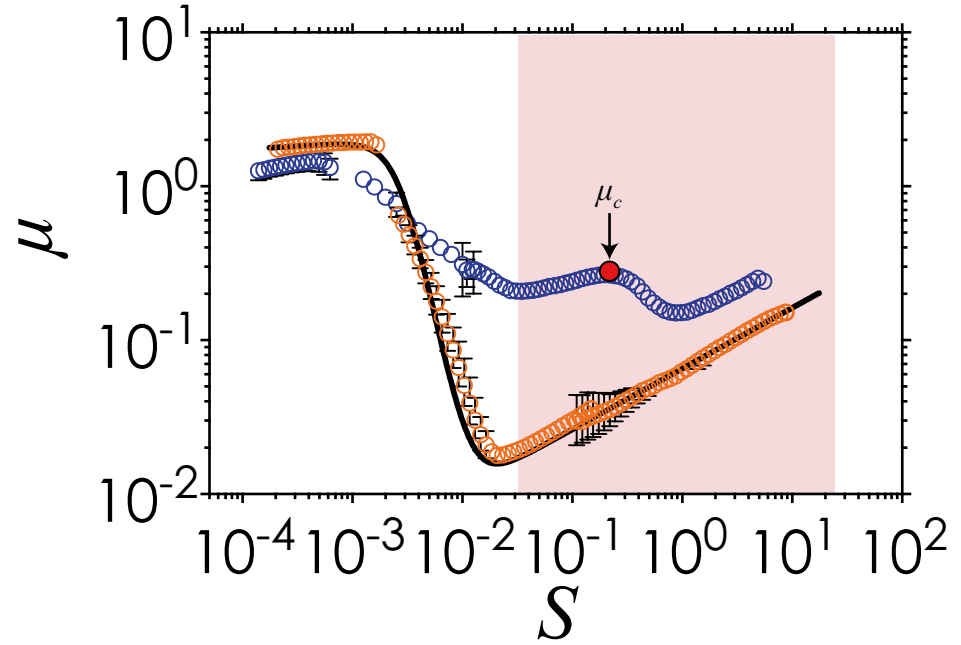
We obtain the static contact area by compressing a fluorescently dyed PDMS ball onto the micropatterned substrates with various  $a$ ,  $b$  and  $c$  at  $F_N=1.5$  N without glycerol. The ball is dyed by dissolving Nile Red in toluene (0.5:99.5% w/w%) and immersing the ball in the dye solution for 12 h. Excess toluene inside the PDMS network is removed by placing the ball in a vacuum chamber for 4 h. After dye transfer by compression, the fluorescent area on the patterned substrates is measured using confocal microscopy (CLSM, Leica SP8) fitted with a 10× dry objective operating in tile stitching mode. The CLSM images show that the contact area on micropatterned surface is within a circle of diameter  $L$  as indicated by the dashed line in Fig. 2(c). A first order assumption is that the effective contact area measured from static contact is similar to the area in lubricated sliding conditions [31]. We define the total area  $A$  as the region enclosed within the dashed circle of Fig. 2(c), and the real contact  $A_a$  as the fluorescent areas. The remaining non-fluorescent area in the circle represents the area of the valleys,  $A_b$ . Using the geometrical parameters in Fig. 1(a), we obtain a relation between the contact area and total area as  $A_a=aA/(a+b)$  and  $A_b=bA/(a+b)$ .

### Theoretical Background

#### The friction peak in EHL

Figure 3 shows a standard Stribeck curve in which the bulk friction coefficient  $\mu$  is plotted as a function of the Sommerfeld number  $S$  for tribopairs in steady state sliding conditions. The non-dimensional Sommerfeld number  $S=U\eta(L^2/\langle h \rangle)/F_N$  scales as the ratio of friction force  $F_S$  to the normal force  $F_N$ . The  $\langle h \rangle$  in the Sommerfeld number represents the average film thickness for all geometries at the micro-to-macro EHL transition point, which is shown in Figs. 6 and 7 for all PDMS-PDMS and PDMS-hydrogel tribopairs. As  $S$  increases, boundary lubrication gives way to EHL and full hydrodynamic lubrication, where the lubricant film fully separates the two solid surfaces. When microscale stripes are present on one or both of the tribopairs, a local peak in the EHL regime appears in the Stribeck curve. No such EHL friction peaks are found in otherwise flat tribopairs. The mechanistic origin of this persistent friction peak ( $\mu_c$ ) is likely due to a micro-EHL to macro-EHL transition [9, 14]. In this work, we analyze  $\mu_c$  as a function of the pattern aspect ratio for the elastomeric tribopairs.

**Fig. 3** Steady state Stribeck curves of flat (orange) and patterned (blue) PDMS-PDMS tribopairs. The pattern dimensions are  $a=25\ \mu\text{m}$ ,  $b=55\ \mu\text{m}$ ,  $c=35\ \mu\text{m}$ . Pink area indicates the EHL regime for flat surfaces and encompasses the micro-EHL to macro-EHL transition for patterned surfaces. Friction peak  $\mu_c$  on patterned curve is highlighted with a red point

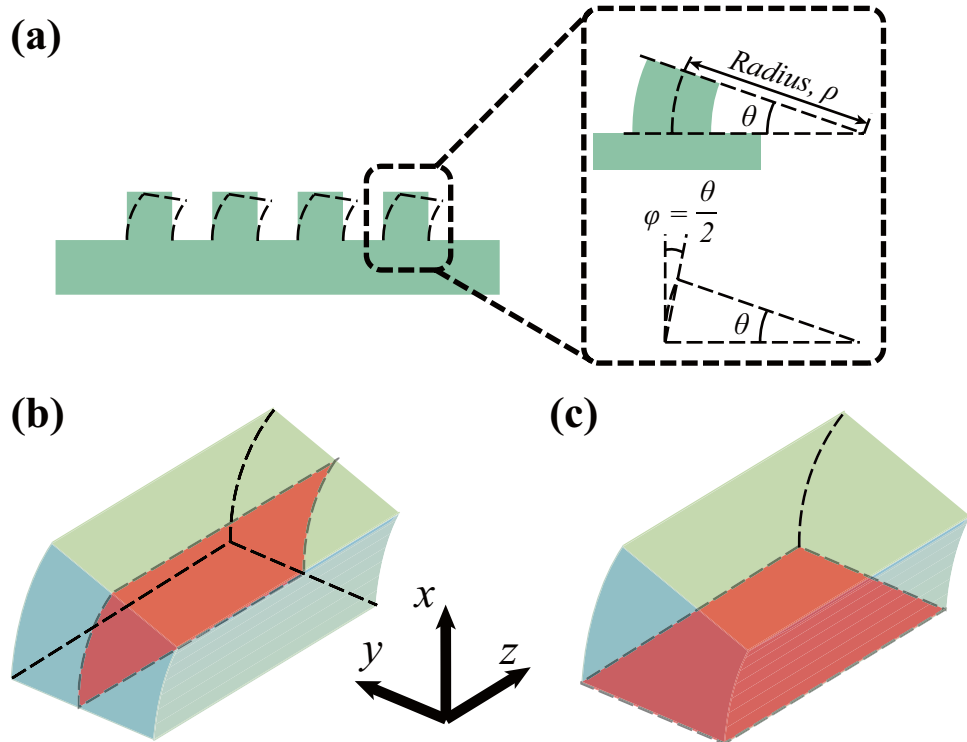


### Bending as a function of the aspect ratio

The aspect ratio  $c/a$  is an essential parameter for estimating the extent of bending under shear. Small values of  $c/a$  indicate short and wide micropatterns in which bending is minor, while large values of  $c/a$  indicate large aspect ratio micropatterns that bend significantly under an applied shear

stress. When high aspect ratio patterns bend, the load-bearing area of the patterns is reduced by a factor that scales with the bending angle  $\theta$  (Fig. 4(a)). Because we are unable to directly measure  $\theta$  at this time, we instead use two separate models based on experimental input to converge at the theoretical value of  $\theta$ . The first method considers each micropattern as a bending cantilever in which material parameters are

**Fig. 4** (a) Sketch of a PDMS patterned surface where the applied shear stress induces bending, where the inset shows relevant geometrical parameters used in the cantilever beam model. (b, c) 3D sketch of a bending pattern indicating the neutral planes in Cartesian coordinates (red)



applied using linear beam theory to obtain  $\theta$  [32]. The second method uses a purely empirical correlation between the EHL friction peak  $\mu_c$  and the geometrical parameter  $a/(a+b)^{0.5}$  that was obtained from our previous study. We assume that the empirical model applies to the patterns in this study because it was generated by statistical modeling of a large number of striped patterns made from different materials [14].

Length scales involved in the bending of soft micropatterns are used in the cantilever bending model to obtain theoretical bending angles. Figure 4(a) defines the bending radius of curvature with respect to the flat surface as  $\rho$ , the bending angle as  $\theta$ , and the deflection angle as  $\varphi = \theta/2$ . The deflection angle  $\varphi$  is an intuitive physical parameter because it represents the extent of bending away from the static pillar. The bending angle  $\theta$  is obtained by assuming each micropattern as an independent beam with small deflections ( $\theta < 30^\circ$ ,  $\varphi < 15^\circ$ ) at the maximum shear velocities tested. We shall revisit this assumption in the data analysis section. The neutral plane, defined as the plane where the bending stress and strain are zero, serves as the reference plane (Fig. 4(b), (c)). The  $x$ -axis is defined from the bottom towards the top of the patterns and it is parallel to the neutral plane before bending occurs. With the  $x$ -axis fixed, the  $y$ - and  $z$ -axes are then settled on the red plane at the fixed end highlighted in Fig. 4(c) where the  $y$ -axis is parallel to the pattern width  $a$  and the  $z$ -axis is orthogonal to the  $y$ -axis. Cartesian coordinates  $(x, y, z)$  are defined with respect to the plane to which the beam is anchored. The bending moment  $M(x)$  and moment of inertia  $I_z$  about the neutral axes are defined as

$$M(x) = -F_S x \quad (1)$$

$$I_z = \frac{La^3}{12} \quad (2)$$

where  $F_S$  is the shear force applied by the rheometer and  $L$  is the diameter of contact area as shown in Fig. 2(c).

It has been shown that linear bending can be assumed if the dimensionless load parameter  $\alpha$  at the free end of the beam is small. This load parameter is defined as [32]

$$\alpha = \frac{F_S c^2}{2EI_z} \quad (3)$$

where  $E = 2$  MPa is the Young's modulus of PDMS [30]. The corresponding bending angle under a specific  $\alpha$  at the limit of small deflection is

$$\theta = \int_0^c \frac{M(x)}{EI_z} dx \quad (4)$$

Belendez et al. compared the cantilever bending deflections obtained from analytical and numerical solutions and showed that when  $\alpha \leq 0.25$  and  $\theta \leq 30^\circ$  ( $\varphi \leq 15^\circ$ ), the assumption of small beam deflection remains valid [32]. We incorporate  $F_s$  from the triborheometer along with material properties into equation (3) to determine  $\alpha$ . If  $\alpha \leq 0.25$ , we then use equation (4) to calculate bending angles for different sized micropatterns and examine the correlation between bending angle and EHL friction. If  $\alpha > 0.25$ , the value of  $\theta$  computed from equation (4) is likely to overestimate the true bending angle. In this case, equation (4) provides an upper limit of  $\theta$ .

To provide independent support for the theoretical  $\theta$  and  $\varphi$  values obtained from equation (4), we use the empirical correlation for generated in our previous work for soft patterns with a range of  $a$  and  $b$  values and a constant value of  $c = 35$   $\mu\text{m}$  ( $c/a < 1.4$ ) [14]. An ordinary linear regression analysis was used to generate the empirical correlation in this study:

$$\mu_c = 0.0695 \frac{a}{\sqrt{a+b}} \quad (5)$$

If we assume that all of the micropatterns from this study were bending from the applied shear stress, then the correlation could be modified to estimate a bending angle. We redefine the geometrical parameters in equation (5) and obtain

$$\mu_c = 0.0695 \frac{a_{\text{eff}}}{\sqrt{a_{\text{eff}}+b}} \quad (6)$$

Here,  $a_{\text{eff}}$  represents the projection of a bending pattern onto the flat substrate as shown in Fig. 5, where the projected length of the raised stripe is related to the bending angle through  $a_{\text{eff}} = a \cos(\theta)$ . The empirical values of  $\theta$  obtained from this method are compared with the

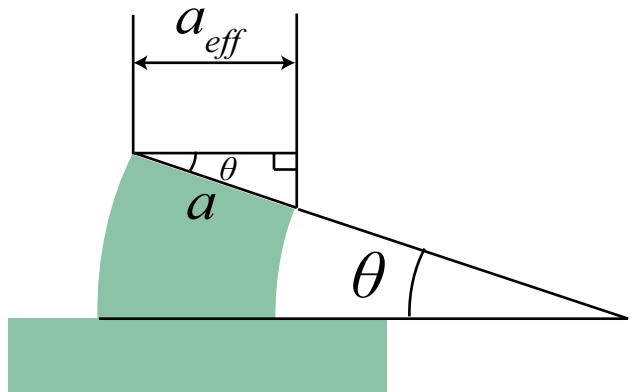


**Fig. 5** Sketch of the projected length of a single micropattern with a reduced effective area for bearing fluid load,  $a_{\text{eff}} \leq a$

theoretical predictions of  $\theta$  from equation (4) for the different aspect ratios used in this study.

## Results and Discussion

### Threshold Aspect Ratio in Bending Patterns

Figure 6 plots  $\mu$  and the lubrication film thickness  $h$  in the EHL regime for patterns with  $\{a=25 \mu\text{m}, b=55 \mu\text{m}, 0.8 \leq c/a \leq 2.0\}$  (set 1, Fig. 6(a), (c)) and  $\{a=55 \mu\text{m}, b=55 \mu\text{m}, 0.4 \leq c/a \leq 0.9\}$  (set 2, Fig. 6(b), (d)) where  $20 \mu\text{m} \leq c \leq 50 \mu\text{m}$ . The film thickness shown in Figs. 6(c) and 5(d) is calculated by adding three individual components:

$$h(U) = h_a(U) + c\epsilon(U) + \Delta h(U) \quad (7)$$

The first term  $h_a(U)$  represents the change in  $h$  as a function of  $S$  and other material properties for flat tribopairs to represent the bulk substrate before texture consideration. The value of  $h_a$  is geometrically modified from correlations of Hamrock and Dowson for flat tribopairs, which perform fairly well in predicting experimental film thickness values in the range of microns [4]. The second term  $c\epsilon(U)$  represents the deformation of micropatterns, and the third term  $\Delta h(U)$  represents the experimentally measured change in  $h$  for microtextured surfaces across all  $S$ . The detailed derivation of  $h$  can be found in ref. [14].

Set 1 patterns (Fig. 6(a), (c)) have larger aspect ratios than set 2 patterns (Fig. 6(b), (d)) and are therefore more prone to

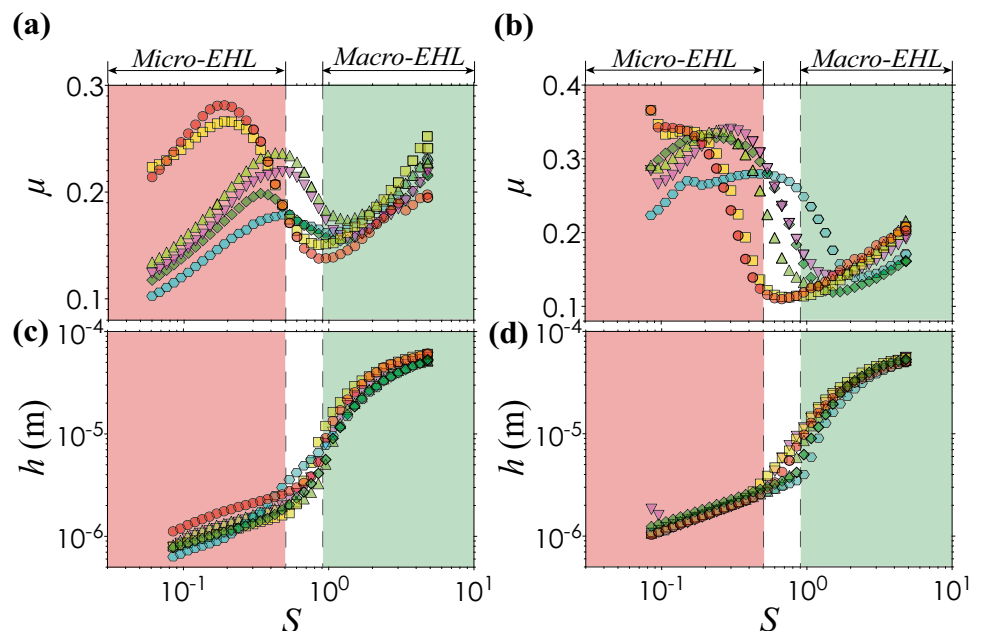
bending. All curves in Fig. 6 demonstrate a similar trend: as  $S$  increases in the micro-EHL regime,  $\mu$  first reaches a local maximum  $\mu_c$ , then decreases to a local minimum indicative of a micro-EHL to macro-EHL transition, and finally increases monotonically in the full hydrodynamic regime at large  $S$ . In the regime where the flow transitions from micro-EHL to macro-EHL, the increases in  $h$  occurs in a monotonic manner with different rate (Fig. 6(c), (d)). The friction peak  $\mu_c$  is consistent with a significant jump in  $h$  at intermediate values of  $S$ . Set 1 shows a range of  $\mu_c$  values between 0.17 and 0.27, while set 2 shows a smaller range of  $\mu_c$  values ranging from 0.27 to 0.33. The  $\mu_c$  peaks occur in a slightly broader range of  $S$  values ( $0.1 < S < 0.9$ ) as compared to the corresponding increases in  $h$ , which are different between samples but occur across a relatively narrow range of  $S$  ( $0.5 \leq S \leq 0.9$ ). We use the jump in  $h$  to demarcate the micro-EHL to macro-EHL transition regime.

The frictional transition from micro-EHL to macro-EHL is not found with flat surfaces as shown in Fig. 3. Furthermore, the value of  $\mu$  for flat surface (Fig. 3) is significantly smaller than that for patterned surfaces (Fig. 6(a), (b)). Such differences could arise from differences in the flow trajectories caused by the presence of the patterned geometries. Earlier work showed that the value of  $h$  is much smaller for patterned surfaces at low sliding speeds [14]. Because the correlation between friction force  $F_S$  and  $h$  is

$$F_S \sim \frac{U\eta}{h} A_a \quad (8)$$

the EHL friction peak for patterned surface would be significantly larger as shown in the inverse scaling between friction

**Fig. 6** (a, c) EHL friction coefficient and film thickness for PDMS-PDMS tribopairs with pattern dimensions  $a=25 \mu\text{m}$ ,  $b=55 \mu\text{m}$  and varying heights. (b, d) EHL friction coefficient and film thickness for PDMS-PDMS tribopairs with pattern dimensions  $a=55 \mu\text{m}$ ,  $b=55 \mu\text{m}$  and varying heights. In (a-d), the pattern heights used are  $c=20 \mu\text{m}$  (red circles),  $c=23 \mu\text{m}$  (yellow squares),  $c=25 \mu\text{m}$  (green triangles),  $c=29 \mu\text{m}$  (purple triangles),  $c=35 \mu\text{m}$  (green diamonds),  $c=50 \mu\text{m}$  (blue hexagons). Red areas indicate micro-EHL and green areas indicate macro-EHL



and  $h$ , which supports our experimental observations that the EHL friction for patterned tribopairs is always higher than that for flat tribopairs.

The observation that  $\mu_c$  changes as a function of  $c/a$  is attributed to the bending of micropatterns as shown in Fig. 1(b). Further analysis of the data in Fig. 6 shows that there are two distinct regimes for which  $\mu_c$  changes. Since the frictional data for tribopairs with substrates made from PEDGA/alginate DN hydrogels still show a frictional peak (Fig. 7), we normalize the friction coefficient, using the same method from ref. [14], as  $\hat{\mu}_c = \mu_c / (E'/E'_{p-p})$  where  $E'$  is the reduced Young's modulus of the tribopair and  $E'_{p-p}$  is the reduced Young's modulus of PDMS-PDMS tribopair, to demonstrate the generality of the bending analysis. Figure 8 shows that the normalized  $\hat{\mu}_c$  of PDMS-PDMS and PDMS-hydrogel tribopairs is independent of  $c/a$  when  $c/a < 0.75$ , while  $\hat{\mu}_c$  decreases with increasing aspect ratio in a power-law fitting where  $\hat{\mu}_c \sim (c/a)^{-0.5}$  when  $c/a > 0.75$ . The distinct separation at  $c/a = 0.75$  indicates that it is the threshold aspect ratio for which bending

contributes significantly to the magnitude of EHL friction peaks in the type of PDMS elastomers used in our study.

In order to extract a physical rationale for the nonlinear decrease in  $\hat{\mu}_c$  when  $c/a > 0.75$ , recall that the projected peak dimension of a bent pattern is  $a_{eff} = a \cos(\theta) \leq a$ . This projected length represents the effective surface area of a bent micropattern that is available for bearing the lubrication fluid load in the micro-EHL regime. We assume that the total contact area  $A$  does not change regardless of the pattern dimensions  $a$  and  $b$ . Furthermore, for small values of  $\theta$ ,  $a_{eff} + b \approx a + b$ . We now substitute the relation

$$\frac{a_{eff}}{\sqrt{a_{eff} + b}} \leq \frac{a}{\sqrt{a + b}} \quad (9)$$

into equation (6) and compare the result with equation (5) to show that  $\hat{\mu}_c$  is reduced by bending, because it reduces the amount of surface area available for bearing the fluid load. Equation (9) highlights the role of  $a$  in decreasing the magnitude of the EHL friction in the power-law fitting regime where  $\theta$  may be large.

Another way to explain the decrease in EHL friction is to consider how the film thickness  $h$  changes with bending micropatterns. In the micro-EHL regime where lubrication flow over the top of the micropatterns support the majority of the normal load, Reynolds' equations state that

$$F_N \sim \frac{U\eta a}{h^2} A_a \quad (10)$$

The value of  $F_N$  is maintained at a constant value of 1.5 N by the rheometer regardless of the aspect ratio of the micropattern. Equating the normal forces for unbent and bending micropatterns suggest that

$$\frac{U\eta a}{h^2} A_a \approx \frac{U\eta a}{h_{eff}^2} A_{eff} \quad (11)$$

where

$$A_{eff} = \left( \frac{a_{eff}}{a_{eff} + b} \right) A \quad (12)$$

Equation (12) suggests that  $A_{eff} < A_a$  when  $\theta$  is large. Substitution of equation (12) into equation (11) indicates that  $h_{eff} < h$ , where  $h_{eff}$  is the effective lubricant film thickness with bending micropatterns.

The data and analysis in this section show that the bending of soft micropatterns is directly influenced by the aspect ratio of the pattern  $c/a$ , such that larger values of  $c/a$  result in larger bending and a reduced value of  $\hat{\mu}_c$ . Lubrication analysis suggests that the decreased EHL friction coefficient is a result of a decreasing lubricant film thickness.

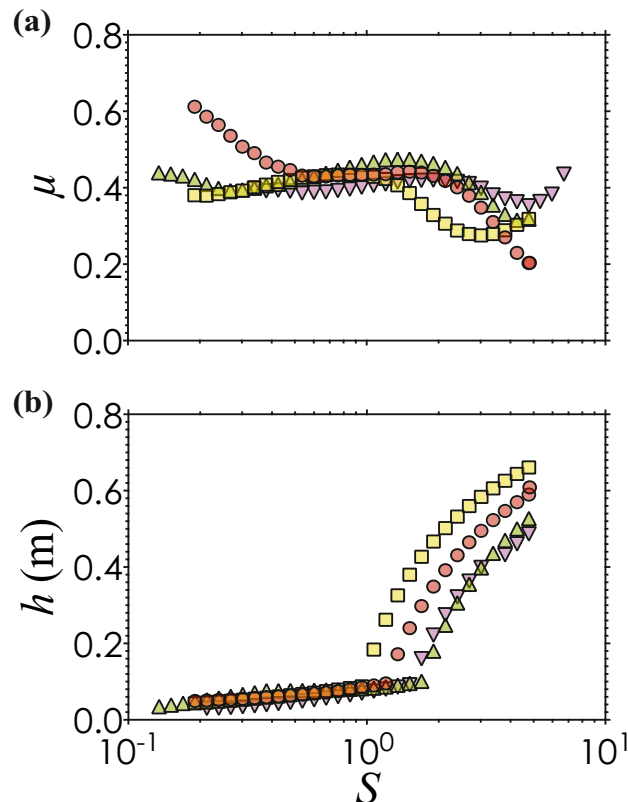
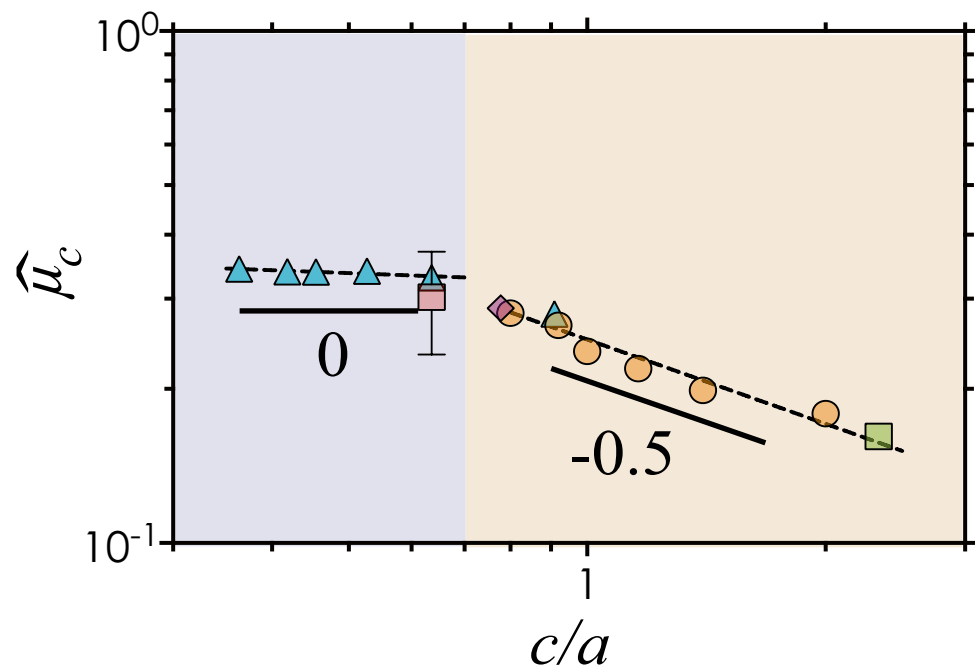


**Fig. 7** (a) EHL tribological data and (b) film thickness  $h$  versus Sommerfeld number,  $S$  on PEDGA/alginate DN hydrogel substrates with pattern dimensions  $a=55\text{ }\mu\text{m}$ ,  $c=35\text{ }\mu\text{m}$  and varying pattern gaps  $b$ . In (a, b), the pattern gaps used are  $b=55\text{ }\mu\text{m}$  (red circles),  $b=75\text{ }\mu\text{m}$  (yellow squares),  $b=100\text{ }\mu\text{m}$  (green triangles),  $b=200\text{ }\mu\text{m}$  (purple triangles)

**Fig. 8** Plot of normalized  $\mu_c$  as a function of  $c/a$ , where purple area represents patterns with small bending angles ( $\theta < 6^\circ$ ) and orange area represents patterns with large bending angles ( $\theta > 6^\circ$ ). Pattern dimensions on PDMS substrates include:  $a = 15 \mu\text{m}$ ,  $b = 55 \mu\text{m}$ ,  $c = 35 \mu\text{m}$  (green);  $a = 25 \mu\text{m}$ ,  $b = 55 \mu\text{m}$ ,  $c = 20, 23, 25, 29, 35, 50 \mu\text{m}$  (orange);  $a = 45 \mu\text{m}$ ,  $b = 55 \mu\text{m}$ ,  $c = 35 \mu\text{m}$ ;  $a = 55 \mu\text{m}$ ,  $b = 55 \mu\text{m}$  (yellow),  $c = 20, 23, 25, 29, 35, 50 \mu\text{m}$  (blue). Pattern dimensions on PEGDA/alginate DN hydrogel substrates are:  $a = 55 \mu\text{m}$ ,  $c = 35 \mu\text{m}$ ,  $b = 55, 75, 100, 200 \mu\text{m}$  (red)



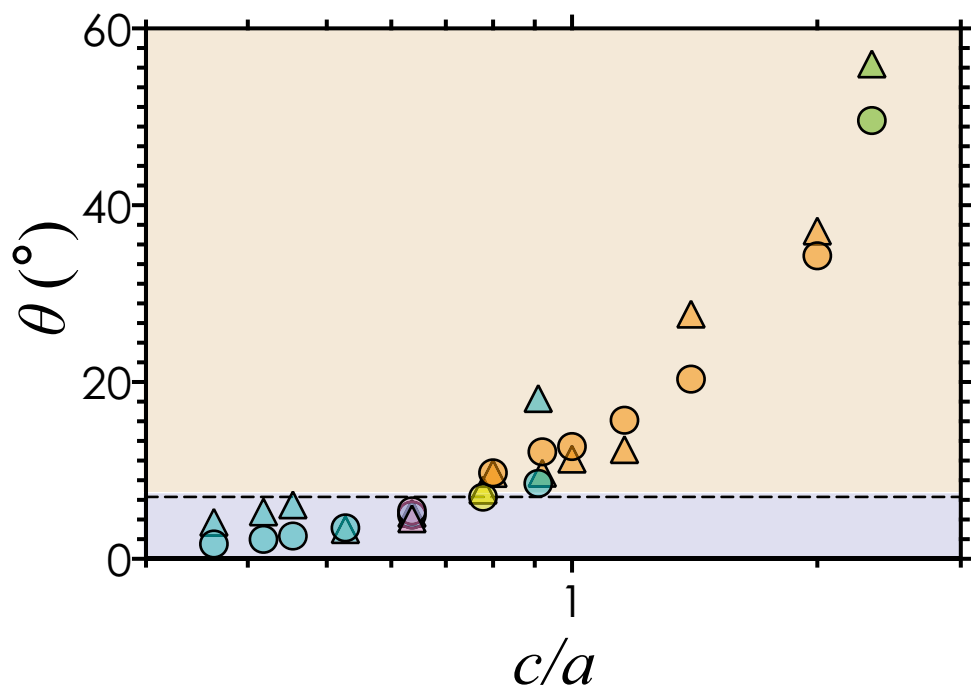
### Comparison of Bending Angles

The dimensionless load parameter  $\alpha$  is computed using equation (3) to determine the validity of the cantilever beam model for estimating  $\theta$ . Recall that the theoretical bending angle from equation (4) overestimates the actual value when  $\alpha \geq 0.25$ . The value of  $\alpha$  for the majority of our experimental data in Fig. 8 is  $< 0.25$ , indicating equation (4) is valid for both set 1

and set 2. For one of the patterns with the highest aspect ratio ( $a = 15 \mu\text{m}$ ,  $c = 35 \mu\text{m}$ ,  $c/a = 2.3$ , green rectangle in Fig. 8), the value of  $\alpha = 0.26$ , suggesting that the theoretical  $\theta$  slightly overestimates the real bending angle. The empirical model in equation (6) is used to provide a parallel comparison of the estimated value of  $\theta$ .

Figure 9 shows the change in bending angle for friction peaks as a function of the pattern aspect ratio using the two

**Fig. 9** Plot of theoretical  $\theta$  as a function of  $c/a$ , where purple area represents patterns with small bending angles ( $\theta < 6^\circ$ ) and orange area represents patterns with large bending angles ( $\theta > 6^\circ$ ). Computed angles are from the cantilever beam model (circles) and the empirical regression developed in ref. [14] (triangles). Pattern dimensions on PDMS substrates include:  $a = 15 \mu\text{m}$ ,  $b = 55 \mu\text{m}$ ,  $c = 35 \mu\text{m}$  (green);  $a = 25 \mu\text{m}$ ,  $b = 55 \mu\text{m}$ ,  $c = 20, 23, 25, 29, 35, 50 \mu\text{m}$  (orange);  $a = 45 \mu\text{m}$ ,  $b = 55 \mu\text{m}$ ,  $c = 35 \mu\text{m}$ ;  $a = 55 \mu\text{m}$ ,  $b = 55 \mu\text{m}$  (yellow),  $c = 20, 23, 25, 29, 35, 50 \mu\text{m}$  (blue). Pattern dimensions on PEGDA/alginate DN hydrogel substrates are:  $a = 55 \mu\text{m}$ ,  $c = 35 \mu\text{m}$ ,  $b = 55, 75, 100, 200 \mu\text{m}$  (red)



different models. As  $c/a$  increases to 0.75, the value of  $\theta$  approaches  $6^\circ$ , which represents the upper limit for which the assumption of linear elasticity is valid. This point coincides with the transition in  $\hat{\mu}_c$  from being independent of  $c/a$  to decreasing as a power-law function (Fig. 8), which further supports our finding that large bending strains in soft pattern cause a reduction in the EHL friction coefficient. Both models provide values of  $\theta$  that are in good agreement with each other, and show that  $\theta$  increases with  $c/a$  as expected for taller patterns. When the aspect ratio increases beyond  $c/a > 0.75$ , the cantilever beam bending model is still able to provide reasonable estimates of the bending and deflection angles ( $\theta \leq 30^\circ$ ,  $\varphi \leq 15^\circ$ ) as shown by Belendez and coworkers [32]. At  $c/a \geq 2.0$ , both models are likely to significantly overestimate the bending angles.

## Conclusions

In this study, we evaluated the bending contribution of soft PDMS and hydrogel microstripes to their EHL tribology by varying the height-to-width aspect ratio,  $c/a$ , while keeping the valley width,  $b$ , constant. A Newtonian lubricant, glycerol, is used to generate fully flooded EHL conditions. The steady state Stribeck curves show that all samples underwent a micro-EHL to macro-EHL transition. It would be interesting and prudent to measure the true film thickness using specialized setups which allow simultaneous imaging of the lubricant film during shear.

Our findings show that the EHL friction peak  $\hat{\mu}_c$  has no dependence on the aspect ratio when  $c/a < 0.75$  but decreases when  $c/a > 0.75$ . Two models are used to explain the decrease in  $\hat{\mu}_c$ : the first uses the cantilever beam model to predict a theoretical bending and deflection angle, and the second uses a purely empirical model we developed previously using a large number of soft micropatterns. Both models consistently support our argument that the increased bending of larger aspect ratio patterns results in a lower effective surface area for bearing the lubrication fluid load, and possibly leads to a reduction in the film thickness. At the threshold value of  $c/a = 0.75$ , the applied shear stresses in the EHL regime cause a bending strain that is sufficiently large to render linear elasticity assumptions invalid. This threshold aspect ratio coincides with the point at which  $\hat{\mu}_c$  is affected by  $c/a$ . The range of aspect ratios studied is limited by experimental instrumentation, specifically related to the optical diffraction effects in photolithography. It would be interesting to obtain structures with larger  $c/a$  values to determine if the decrease in EHL friction peak is monotonic with tall and thin structures.

Although the elastic compression of a soft surface is factored into classical tribology through Hertzian and adhesive contact models, bending has not been a focus because of the relatively rigid nature of traditional tribopairs.

Results from this study would be applicable to the lubricated friction of human fingertips and texture perception aided by papillae in the tongue. These haptic processes often involve sliding conditions similar to those in our study, suggesting the combination of bending mechanics with tribological modeling is likely to be very impactful to soft robotics [14], haptic devices [33], and biomechanics [34].

**Acknowledgements** Y. P., C. M. S., C.N.H. and L. C. H. were funded by North Carolina State University startup funds, the AAAS Marion Milligan Mason Award, and the National Science Foundation (CBET-2042635).

## Declarations

**Conflict of Interest** The authors report no conflict of interest.

## References

1. Dowson D (2012) Bio-tribology. *Faraday Discuss* 156(1):9–30. <https://doi.org/10.1039/C2FD20103H>
2. Stokes JR, Boehm MW, Baier SK (2013) Oral processing, texture and mouthfeel: From rheology to tribology and beyond. *Curr Opin Colloid Interface Sci* 18(4):349–359. <https://doi.org/10.1016/j.cocis.2013.04.010>
3. Davies HS, Débarre D, El Amri N, Verdier C, Richter RP, Bureau L (2018) Elastohydrodynamic lift at a soft wall. *Phys Rev Lett* 120(19):198001. <https://doi.org/10.1103/PhysRevLett.120.198001>
4. Hamrock BJ, Dowson D (1977) Isothermal Elastohydrodynamic lubrication of point contacts: part III—fully flooded results. *J Lubr Technol* 99(2):264–275. <https://doi.org/10.1115/1.3453074>
5. Saintyves B, Jules T, Salez T, Mahadevan L (2016) Self-sustained lift and low friction via soft lubrication. *Proc Natl Acad Sci USA* 113(21):5847–5849. <https://doi.org/10.1073/pnas.1525462113>
6. Wang Y, Dhong C, Frechette J (2015) Out-of-contact elastohydrodynamic deformation due to lubrication forces. *Phys Rev Lett* 115(24):248302. <https://doi.org/10.1103/PhysRevLett.115.248302>
7. Stachowiak G, Batchelor AW (2014) Elastohydrodynamic lubrication. In: *Engineering tribology*, 4th edn. Butterworth-Heinemann
8. Bonnevie ED, Delco ML, Galessio D, Secchieri C, Fortier LA, Bonassar LJ (2017) Sub-critical impact inhibits the lubricating mechanisms of articular cartilage. *J Biomech* 53:64–70. <https://doi.org/10.1016/j.jbiomech.2016.12.034>
9. Scaraggi M, Carbone G, Dini D (2011) Experimental evidence of micro-EHL lubrication in rough soft contacts. *Tribol Lett* 43(2):169–174. <https://doi.org/10.1007/s11249-011-9794-6>
10. Varenberg M, Gorb SN (2009) Hexagonal surface micropattern for dry and wet friction. *Adv Mater* 21(4):483–486. <https://doi.org/10.1002/adma.200802734>
11. Drotlef DM, Stepien L, Kappl M, Barnes WJP, Butt HJ, del Campo A (2013) Insights into the adhesive mechanisms of tree frogs using artificial mimics. *Adv Funct Mater* 23(9):1137–1146. <https://doi.org/10.1002/adfm.201202024>
12. Etsion I, Burstein L (1996) A model for mechanical seals with regular microsurface structure. *Tribol Trans* 39(3):677–683. <https://doi.org/10.1080/10402009608983582>
13. Gropper D, Wang L, Harvey TJ (2016) Hydrodynamic lubrication of textured surfaces: A review of modeling techniques and key

findings. *Tribol Int* 94:509–529. <https://doi.org/10.1016/j.triboint.2015.10.009>

14. Peng Y, Serfass CM, Hill CN, Hsiao LC (2019) Lubricated friction of textured soft substrates. *arXiv preprint arXiv*: 190906431
15. Dowson D, Higginson G (1959) A numerical solution to the elasto-hydrodynamic problem. *J Mech Eng Sci* 1(1):6–15. [https://doi.org/10.1243/JMES\\_JOUR\\_1959\\_001\\_004\\_02](https://doi.org/10.1243/JMES_JOUR_1959_001_004_02)
16. Grubin A (1949) Fundamentals of the hydrodynamic theory of lubrication of heavily loaded cylindrical surfaces. In: *Investigation of the contact of machine components*. Central Scientific Research Institute for Technology and Mechanical Engineering
17. Vinogradova OI, Yakubov GE (2006) Surface roughness and hydrodynamic boundary conditions. *Phys Rev E* 73(4):045302. <https://doi.org/10.1103/PhysRevE.73.045302>
18. Pilkington GA, Gupta R, Fréchette JL (2016) Scaling hydrodynamic boundary conditions of microstructured surfaces in the thin channel limit. *Langmuir* 32(10):2360–2368. <https://doi.org/10.1021/acs.langmuir.5b04134>
19. Lauga E, Pipe CJ, Le Révérend B (2016) Sensing in the mouth: a model for filiform papillae as strain amplifiers. *Front Phys* 4:35. <https://doi.org/10.3389/fphy.2016.00035>
20. Thomazo J-B, Contreras Pastenes J, Pipe CJ, Le Révérend B, Wandersman E, Prevost AM (2019) Probing in-mouth texture perception with a biomimetic tongue. *J R Soc Interface* 16(159):20190362. <https://doi.org/10.1098/rsif.2019.0362>
21. Vogel S (1989) Drag and reconfiguration of broad leaves in high winds. *J Exp Bot* 40(8):941–948. <https://doi.org/10.1093/jxb/40.8.941>
22. Alvarado J, Comtet J, de Langre E, Hosoi A (2017) Nonlinear flow response of soft hair beds. *Nature Phys* 13(10):1014–1019. <https://doi.org/10.1038/nphys4225>
23. Duprat C, Berthet H, Wexler JS, Du Roure O, Lindner A (2015) Microfluidic *in situ* mechanical testing of photopolymerized gels. *Lab on a Chip* 15(1):244–252. <https://doi.org/10.1039/C4LC01034E>
24. Wexler JS, Trinh PH, Berthet H, Quennouz N, Du Roure O, Huppert HE, Lindner A, Stone HA (2013) Bending of elastic fibres in viscous flows: the influence of confinement. *J Fluid Mech* 720:517–544. <https://doi.org/10.1017/jfm.2013.49>
25. Young Y-N, Downs M, Jacobs CR (2012) Dynamics of the primary cilium in shear flow. *Biophys J* 103(4):629–639. <https://doi.org/10.1016/j.bpj.2012.07.009>
26. Thomazo J-B, Lauga E, Révérend BL, Wandersman E, Prevost AM (2020) Collective stiffening of soft hair assemblies. *Phys Rev E* 102(1):010602. <https://doi.org/10.1103/PhysRevE.102.010602>
27. Axtmann G, Hegner F, Brücker C, Rist U (2016) Investigation and prediction of the bending of single and tandem pillars in a laminar cross flow. *J Fluids Struct* 66:110–126. <https://doi.org/10.1016/j.jfluidstructs.2016.07.017>
28. Du P, Lin I-K, Lu H, Zhang X (2010) Extension of the beam theory for polymer bio-transducers with low aspect ratios and viscoelastic characteristics. *J Micromech Microeng* 20(9):095016. <https://doi.org/10.1088/0960-1317/20/9/095016>
29. Skotheim JM, Mahadevan L (2005) Soft lubrication: The elasto-hydrodynamics of nonconforming and conforming contacts. *Phys Fluids* 17(9):092101. <https://doi.org/10.1063/1.1985467>
30. Johnston I, McCluskey D, Tan C, Tracey M (2014) Mechanical characterization of bulk Sylgard 184 for microfluidics and micro-engineering. *J Micromech Microeng* 24(3):035017. <https://doi.org/10.1088/0960-1317/24/3/035017>
31. Pitenis AA, Urueña JM, McGhee EO, Hart SM, Reale ER, Kim J, Schulze KD, Marshall SL, Bennett AI, Niemi SR (2017) Challenges and opportunities in soft tribology. *Tribol Mater Surf Interfaces* 11(4):180–186. <https://doi.org/10.1080/17515831.2017.1400779>
32. Beléndez T, Neipp C, Beléndez A (2002) Large and small deflections of a cantilever beam. *Eur J Phys* 23(3):371–379. <https://doi.org/10.1088/0143-0807/23/3/317>
33. Shao YT, Hayward V, Visell Y (2020) Compression of dynamic tactile information in the human hand. *Sci Adv* 6(16):eaaz1158. <https://doi.org/10.1126/sciadv.aaz1158>
34. Hellman RB, Chang E, Tanner J, Tillery SIH, Santos VJ (2015) A robot hand testbed designed for enhancing embodiment and functional neurorehabilitation of body schema in subjects with upper limb impairment or loss. *Front Hum Neurosci* 9. <https://doi.org/10.3389/fnhum.2015.00026>

**Publisher's Note** Springer Nature remains neutral with regard to jurisdictional claims in published maps and institutional affiliations.